

# Small-angle pump–probe studies of photoexcited nanoparticles

Anton Plech,<sup>a\*</sup> Vassilios Kotaidis,<sup>a</sup> Konstantin Istomin<sup>a</sup> and Michael Wulff<sup>b</sup>

<sup>a</sup>Fachbereich Physik der Universität Konstanz, D-78457 Konstanz, Germany, and <sup>b</sup>European Synchrotron Radiation Facility, BP 220, 38043 Grenoble, France.

E-mail: anton.plech@uni-konstanz.de

X-ray scattering experiments on femtosecond laser-excited gold nanoparticle suspensions are presented. It is shown that the time-resolved pump–probe technique using the X-ray pulse structure at synchrotron sources is capable of resolving structural dynamics on the nanometer scale to high precision. The estimation of X-ray flux density allows the projection of experiments on an X-ray free-electron laser probing single nanoparticles in a one-shot exposure.

**Keywords:** small-angle scattering; nanoparticles; femtosecond laser; picosecond time resolution.

## 1. Introduction

Pump–probe studies of structural relaxations in condensed matter have been successfully applied to scattering experiments in single crystals (Siders *et al.*, 1999; Collet *et al.*, 2003), powders (Techert *et al.*, 2001) and liquid solutions (Plech *et al.*, 2004; Ihee *et al.*, 2005), and spectroscopic techniques have been used in solution studies (Chen *et al.*, 2001; Saes *et al.*, 2003). By exciting the sample using an ultrafast laser pulse and probing change scattering from this perturbation at defined time delay with short X-ray pulses, it has become possible to determine the pathways of ultrafast phase transitions (Rousse *et al.*, 2001), the metabolic pathway of photolyzed biomolecules (Schotte *et al.*, 2003) or chemical bond kinetics on atomic length scales (Cao *et al.*, 1999). Besides the short-range correlations that are probed directly by hard X-rays, meso-scale relaxations, particularly in nanomaterials, are characterized by ultrafast dynamics. They have been predominantly accessed by ultrafast optical pump–probe techniques (Link & El-Sayed, 2000).

Recently we reported on a femtosecond laser excitation study of nanoparticle suspensions, where the melting process (Kotaidis *et al.*, 2006), near-field ablation (Plech *et al.*, 2006) and the reaction of the liquid around the particles (Plech *et al.*, 2005) could be resolved to 100 ps. The ultrafast heating of the latter leads to explosive boiling of the water shell close to the particles and the observation of nanoscale vapor bubbles (Kotaidis & Plech, 2005).

In this communication we describe the potential of time-resolved small-angle X-ray scattering (SAXS) techniques for probing nanoscale structure relaxations. An outlook is given on the relevance for future studies with free-electron lasers with their orders-of-magnitude larger X-ray flux.

## 2. Experimental set-up

Laser-pump–X-ray-probe studies exploit the fact that the X-ray emission from insertion devices at synchrotrons such as the European Synchrotron Radiation Facility (ESRF) is pulsed. The accelerating field for the electron bunches in the ring and the machine parameters define the pulse lengths, which vary typically from 50 to 200 ps depending on the charge of the electron bunch. A technical description of the set-up at beamline ID09B at the ESRF is given by Schotte *et al.* (2002).

A femtosecond laser system [Ti:sapphire regenerative amplifier based on a coherent oscillator (MIRA) and a Ti:sapphire amplifier from Spectra (Hurricane)] is synchronized to the time structure of the X-rays. This is achieved by synchronizing the oscillator to the RF field of the storage ring and amplifying a chosen femtosecond pulse that is synchronous to the X-ray pulses used for the scattering study. The amplifier runs at 986.3 Hz, which is a subharmonic of the RF frequency of the storage ring. At the same time the X-ray repetition frequency is at least 354 kHz, corresponding to a single electron bunch circulating in the ring, or a multiple of that if more bunches are present. An X-ray pulse selector therefore has to isolate single pulses at 986.3 Hz to allow stroboscopic data acquisition by the (slow) detector. This selector (chopper) consists of an in-vacuum titanium triangle with a tunnel carved along one side. It rotates at supersonic speed at the edge ( $600 \text{ m s}^{-1}$ ). The tunnel has a spatially varying gap which defines the opening time of the chopper. In the 16 bunch mode used in the present study the bunches are separated by 176 ns. This defines the required opening time of the rotating chopper to isolate a single X-ray pulse from the two adjacent pulses. The goal can be achieved using a tunnel

height of 0.145  $\mu\text{m}$ . At the same time an upstream toroidal focusing mirror with platinum coating provides an X-ray focus as small as 80  $\mu\text{m}$  in height, in order to avoid transmission losses in the chopper tunnel.

One key to successful experiments at this beamline is the use of the full X-ray spectrum from an in-vacuum undulator (Pollack *et al.*, 2001; Plech *et al.*, 2002). It emits one single line in the low-energy spectrum (presently 17 mm period with smallest gap of 6 mm and peak energy of 15 keV). For liquid scattering experiments the magnetic gap is normally relaxed towards a peak energy of around 18 keV to increase the range in scattering vector  $Q$  and to further reduce the contamination from higher harmonics. The gap opening also serves to reduce the heat load on the chopper, which has a weak heat exchange owing to its operation in a vacuum and the levitating magnetic bearings. As explained below, we have modified the typical settings towards smaller magnetic gaps to reduce the energy of the X-ray to gain resolution at low scattering vector  $Q$ . The lower energy translates into a larger accessible length scale in real space for SAXS. The heat load has been reduced by using a narrow vertical primary slit (0.15 mm, *versus* 0.45 mm of the full emission cone) and aluminium filters. Both serve to narrow the spectrum at the fundamental by reducing the off-axis contributions and by absorbing the low energies in the filter. The resulting profile of the spectrum is  $\lambda$ -shaped with a sharp cut-off at 17.1 keV and a width (full width at half-maximum) of 2.6% (see Fig. 1). The resulting heat load on the chopper is 4 W at 100 mA ring current, the maximum tolerable for the long time operation of the chopper.

The sample consisted of size-selected gold nanoparticles suspended in water. They had been prepared by the Turkevich citrate reduction method (Turkevich *et al.*, 1951; Kimling *et al.*, 2006). Starting from a solution of 1.2 mM gold hydrochlorate resulted in particles of diameter 38 nm with a size dispersion of 13%. The liquid was circulated in a glass X-ray capillary (Hilgenberg, diameter 0.3 mm, wall thickness 10  $\mu\text{m}$ ) which crossed the interaction point of the laser and X-ray beam. The laser beam was further focused by the curvature of the capillary, which had been accounted for by placing the capillary in the diverging part of the beam behind the focus.

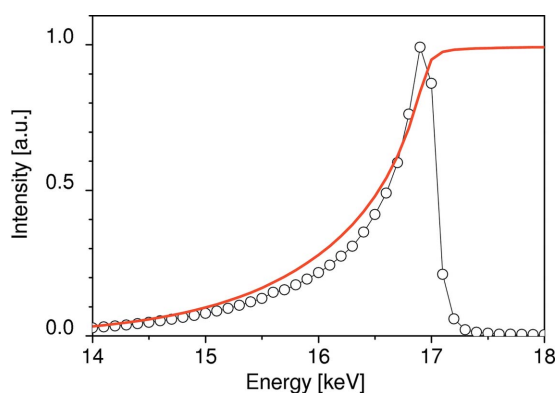


**Figure 1**

Circles: spectrum of the first harmonic of the undulator with its 2.6% bandwidth achieved by reducing the input aperture and using an aluminium filter. The red line represents the flux integral below a given energy.

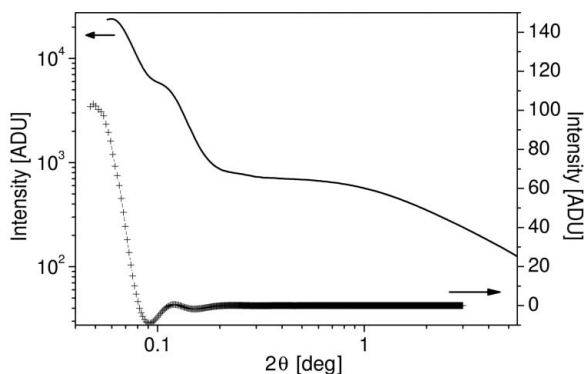
Additionally, the optical density of the sample caused a fluence reduction with increasing penetration of the laser into the slab, which counterbalances the focusing effect. We estimate a residual fluence increase with sample depth of 15% (Kotaidis *et al.*, 2006). Owing to the irreversible nature of the excitation, care was taken to expose every portion of the sample to a single pair of laser and X-ray pulses.

A CCD detector (MarCCD, Mar Research, with 133 mm diameter and  $2048 \times 2048$  pixels) recorded the scattering at a distance of 630 mm. A tungsten cylinder of diameter 1 mm served as a beam block for the transmitted X-ray beam. Consequently, SAXS could be recorded with a lower limit in scattering vector  $Q = 4\pi/\lambda \sin(2\theta/2)$  of  $0.007 \text{ \AA}^{-1}$ . This lower limit is not purely geometrical, since contamination in the wings of the primary beam might dominate for weakly scattering samples. The SAXS set-up is very basic in the sense that no evacuated flight tube was used and the beam-defining slits were not optimized for SAXS. One slit after the toroidal mirror (22 m upstream of the sample) is used to clean up the beam. At the same time the chopper (1 m upstream of the sample) has a similar function. Conversely, it can cause additional scattering if not synchronized properly, owing to scattering from the inclined side walls of the channel. Finally, a beam-defining slit is used at 60 cm followed by a clean-up pinhole 25 mm before the sample. In the pump-probe study the laser action can be used to discriminate between signal and background. Therefore exposures are recorded with variable X-ray laser delay  $\tau$ . One exposure with a negative delay [ $S(Q, \tau < 0)$ ], whereby the X-ray pulse arrives at the sample before the laser, is followed by a positive delay [ $S(Q, \tau > 0)$ ] with the X-ray pulse probing the laser-induced changes. By interleaving both measurements and taking the difference,  $\Delta S(Q, \tau) = S(Q, \tau > 0) - S(Q, -1 \text{ ns})$ , the background is efficiently removed. Drifts can be rejected by longer sequences and a corresponding protocol.

As no rapid and precise intensity monitor exists for these studies, the data evaluation protocol included the normalization of the pairs of curves. The scattering intensity at large  $Q$  was used as a normalization value. This range was unperturbed by the mesoscale relaxations at the low  $Q$  investigated here. A last step consisted of taking the azimuthal space angle corrected average of the two-dimensional data (*Fit2D*; Hammersley *et al.*, 1996). Fig. 2 displays the full intensity on the detector and a typical difference curve representing a given X-ray/laser delay. The full curve is characterized by small-angle scattering from the particles at low  $Q$ , with a characteristic form factor minimum around  $0.1 \text{ \AA}^{-1}$ . The scattering is dominated by air and capillary scattering at larger  $Q$ , as tested with the empty capillary. By contrast, the difference in scattering is attributed entirely to the laser-induced structural dynamics.

### 3. Structure function in SAXS and resolution considerations

In the present experiment we deal with initially spherical gold colloids at low particle concentration (1–5 nM). The particles


**Figure 2**

Scattered intensity as a function of  $Q$  for a typical 3 s exposure of the sample together with the difference scattering obtained after subtracting data of a negative (−1 ns) from a positive (300 ps) delay for 38 nm particles excited with  $1270 \text{ J m}^{-2}$ .

can change size through reversible or non-reversible reactions (ablation of material from the surface in the latter case). Additionally, the explosive boiling of the water phase close to the particles can create a layer of reduced density around each individual particle, which will be a function of laser fluence and time.

Generally the scattering yield from a small object in an X-ray beam of flux density  $I_0$  is described by the volume integral over the (electron) density contrast  $\Delta\rho(\mathbf{r})$  and the number of objects  $N$ ,

$$I(Q) \propto I_0 N \left| \int_V \Delta\rho(\mathbf{r}) \exp(iQr) d\mathbf{r} \right|^2 \quad (1)$$

$$= I_0 N S(Q) \quad (2)$$

$$\propto NV^2 (\Delta\rho)^2 F(Q, R)^2, \quad (3)$$

where (3) is the result for an object of homogeneous density  $\Delta\rho$  and volume  $V$  and the structure function as an integral of the phase  $\exp(iQr)$  over the shape.

The structure function  $S(Q)$  for a core–shell system with spherical symmetry has been calculated according to

$$S(Q) = \left[ (4\pi/3)(\rho_{\text{shell}} - \rho_{\text{water}})R_{\text{shell}}^3 F(Q, R_{\text{shell}}) + (4\pi/3)(\rho_{\text{part}} - \rho_{\text{shell}})R_{\text{part}}^3 F(Q, R_{\text{part}}) \right]^2, \quad (4)$$

$$F(Q, R_i) = 3[\sin(QR_i) - (QR_i)\cos(QR_i)]/(QR_i)^3. \quad (5)$$

$F(Q, R_i)$  is the structure function for a homogeneous sphere of radius  $R_i$ , where  $i$  is set by the radii of the particle core, or the shell (vapor in this case), with electron density  $\rho_i$ .

An ensemble of particles is described by a convolution of the scattering function with the particle size distribution. A Gaussian distribution is typically taken, but there exist analytical formulae of core–shell systems, such as the Schulz–Flory distribution (Wagner, 2004). Another way of treating objects with spherical symmetry is to use the kinematic formula of the radial density distribution  $\rho(R)$  (Dingenouts *et al.*, 1999),

$$S(Q) = \left| 4\pi \int_0^\infty [\rho(R) - \rho_{\text{water}}] \frac{\sin QR}{QR} R^2 dR \right|^2. \quad (6)$$

It has the advantage of allowing arbitrary density profiles, particularly for adjusting the density crossover from the core to the shell and the shell to the medium independently. For our systems the above-mentioned descriptions are equivalent.

In Fig. 3 the structure function for a homogeneous sphere of radius 19 nm has been calculated from equation (5) and after convolution with a Gaussian size distribution with 8% standard deviation. Additionally, the convolution of the structure function with the X-ray line shape is shown. It follows that the smearing from the polychromatic spectrum is of the same magnitude as the size distribution used (for the first two minima). At larger  $Q$ , however, the size dispersion damps the oscillations strongly, while the energy spread causes a constant smearing. Moreover, size dispersion tends to shift the minima to lower  $Q$ , as the larger particles have a higher weight owing to the volume term in equation (3). In conclusion, the broadening effects from size dispersion and polychromaticity on the final structure function should be treated independently to avoid systematic errors. The use of bandwidth-optimized multilayer mirrors can reduce the energy spread and provide a more symmetric energy distribution around the center energy for future SAXS studies.

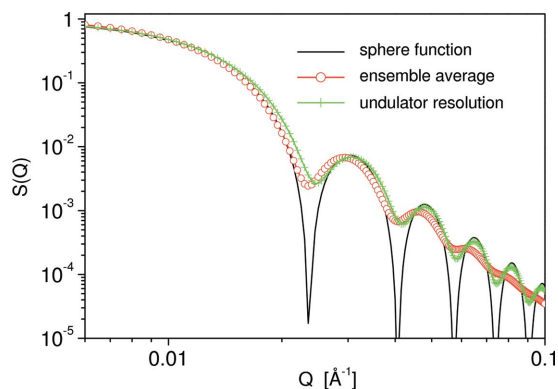
All the above considerations apply for a symmetrical object or at least for a rotationally disordered ensemble of objects. For an ellipsoidal object in particular, the anisotropic SAXS formulae can be generalized by using a scaled  $Q_y$  and  $Q_z$  projection, while keeping constant the limiting intensity at  $Q = 0$  (Guinier & Fournet, 1955; Plech *et al.*, 2006). This is done by replacing  $QR$  in (5) by

$$X(Q_y, Q_z) = [Q_y^2 R^2 + Q_z^2 (\chi R)^2]^{1/2}, \quad (7)$$

with  $\chi$  being the relative change of the shorter axis of an oblate rotational ellipsoid relative to the longer axes or to the initial sphere.

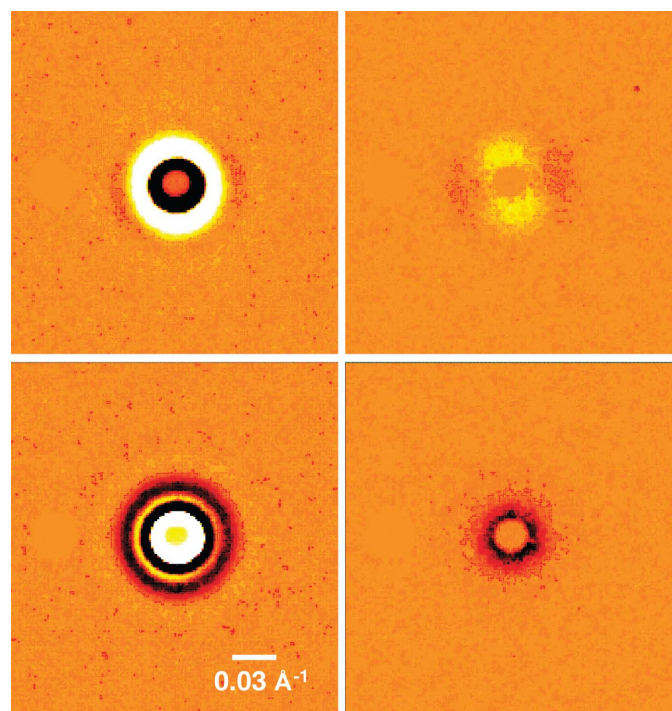
#### 4. SAXS data and simulation

The images in Fig. 4 show typical distributions of difference scattering in the central part of the detector following laser excitation. The individual images show the situation at short delays, where a vapor bubble exists around the hot gold particles, and at a microsecond delay, where all transient phenomena in the liquid have decayed out. The upper images are taken at low laser fluence, just above the threshold for bubble nucleation, where the particle core is still solid. At a delay of 300 ps a concentric ring with slight ellipticity can be observed, while at 1  $\mu\text{s}$  a weaker dipolar change of the scattering distribution remains. This reflects the interpretation that mass removal from the gold particles induces an elongated particle shape. The vertical axis of the pattern coincides with the laser polarization. The laser field causes a plasmonic excitation of the electrons and a field enhancement at the poles. This anisotropy adds to the isotropic signal of the vapor


**Figure 3**

Calculated structure function  $F(Q)^2$  for a homogeneous sphere of radius 19 nm (line), together with the ensemble averaged structure function of width 8% (standard deviation) as circles. Additionally the convolution with the undulator energy spread is shown (crosses).

bubble also at 300 ps. At high laser fluence the patterns are isotropic with a modulation of the difference scattering with much higher frequency at 300 ps, reflecting the increased bubble size after stronger heating. At 1  $\mu$ s there is still a reduction of scattering in the forward direction around the beam block, showing a reduced particle size. The particles here have gone through the liquid state, causing the relaxation to spherical symmetry through the surface tension. It should be emphasized that the anisotropic scattering pattern persists on this long time scale. This can be understood by calculating the rotation relaxation time of a sphere in a liquid (Debye–Stokes–Einstein equation) (Debye, 1929)

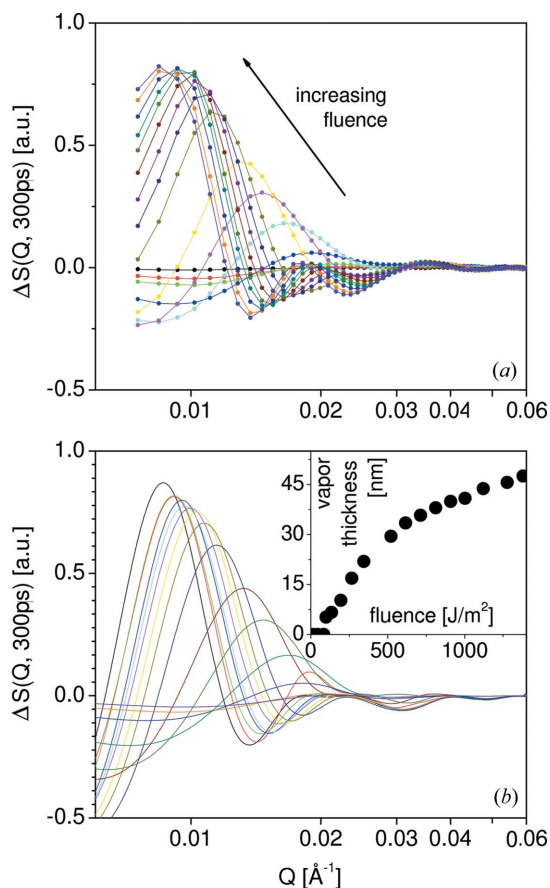

**Figure 4**

False-color plot of the difference intensity for 300 ps (left), 1  $\mu$ s (right), low laser fluence (top) and high laser fluence (bottom). Lighter colours (yellow-white) indicates intensity increase, while darker colours (brown-black) show areas of intensity decrease.

$$\tau_{\text{rot}} = \eta V / k_B T, \quad (8)$$

where  $\eta$ ,  $V$  and  $k_B T$  are the liquid viscosity, particle volume and thermal energy, respectively. For gold particles in water at a temperature at or above room temperature, one obtains a characteristic time scale of about 10  $\mu$ s, which depends inversely on the cube of the particle size. It should be stressed that in ultrafast pump–probe experiments any nanometer-sized object that suffers anisotropic excitation behavior may display its anisotropic fingerprints on the picosecond to nanosecond time scale.

The scattering change due to bubble formation will now be analyzed by applying the core–shell model to the particle–bubble unit. The laser fluence has been changed at constant time delay in small steps to resolve the energetics of the reaction. Fig. 5 shows a sequence of one-dimensional difference scattering functions with increasing laser fluence (following the arrow). There is a prominent maximum at low  $Q$ , eventually followed by several further undulations. This oscillatory structure shifts to even lower  $Q$ . This signal can be satisfactorily reproduced by fits of the data with a gold core in the center of a vapor sphere with a diameter of a few tens of


**Figure 5**

(a) Difference scattering function  $\Delta S(Q)Q^2$  for a set of different laser fluences for a 300 ps delay. With increasing fluence the maximum shifts to lower  $Q$ . The scattering is weighted by  $Q^2$  in order to amplify the modulations at high  $Q$ . (b) Simulations of the curves above for adapted density distributions in a core–shell system. The inset shows the radius of the vapor bubble around the particles as a function of laser fluence. At a fluence below 150  $\text{J m}^{-2}$ , no bubbles are seen.

nanometers. The density of the vapor blanket had to be set to zero, except for the three lowest fluence values. At these curves, either a bubble can be postulated only to a small fraction of the particles, or only a small density reduction around all particles should be present. This is the region where the heat transfer from the hot particles to the liquid surrounding is regular and below the threshold of bubble formation. Above  $150 \text{ J m}^{-2}$ , the bubble signature is clearly identified and the bubbles grow in size with increased fluence. Small-angle scattering can indeed give the proof for a well defined sharp vapor–liquid interface, even for very small bubbles. The discontinuities in heat transfer (Hu *et al.*, 2004; Kotaidis *et al.*, 2006) and transient laser signals are not just gradual density changes, such as thermal lensing caused by heated liquid around the nanoparticles, as has been proposed to explain the transient change of optical transmission to laser-excited silver sols (Maillard *et al.*, 2004).

The details of the modulations could only be reproduced by including two structural features. First, the particles suffer a size reduction in agreement with the observed ablation process. Second, the width of the size distribution for the particle core has to be enlarged from 12% to 17%, while the size distribution for the outer radius of the vapor shell is always in the range 15–20%. The increased dispersion of the particle size could be a remnant of the anisotropic particle shape that changes the sphericity of the particles. The size of the vapor bubble is shown as an inset in Fig. 5(b), displaying a threshold around  $150 \text{ J m}^{-2}$  and subsequently growing monotonically with fluence.

The bubble formation is a threshold process, involving rapid superheating of the liquid up to the spinodal line. The ability to resolve the phase explosion both in time and in space will allow the mechanism of the phase transition and nucleation theory to be understood in more detail. Laser excitation of nanoparticles is discussed as a nanoscale tool in biological applications (Pitsillides *et al.*, 2003).

## 5. Flux considerations and projection to XFEL experiments

Present day experiments can reveal an important part of the kinetics of nanoscale reactions in the condensed phase on an ultrafast time scale. In contrast, the elementary steps of the ablation, and explosive boiling transformation, would require methods to be used with a time resolution that allows the motion to be tracked on the 100 fs time scale. As the present system requires both a high flux and a considerable angular collimation, laser plasma-based X-ray sources will not be compatible. The development of free-electron lasers based on the self-amplified stimulated emission (SASE) of X-ray light promises to open a new dimension for the study of dynamics (Arthur *et al.*, 2002; Aghababayan *et al.*, 2006). The current data are limited by time resolution, ensemble averaging over non-identical particles and fluence averaging over multiple laser excitation shots. The SASE radiation promises to deliver  $10^{12}$  photons at 12.4 keV in one 100 fs burst ( $10^{13}$  at 3.1 keV) (Aghababayan *et al.*, 2006) for the European XFEL proposal.

**Table 1**

Photon numbers and cross sections of SAXS experiments on gold nanoparticles.

	Present experiment	XFEL
Photons in one pulse	$5 \times 10^8$	$10^{12}$
Photon energy	16.7 keV	12.4 keV
X-ray size	$0.1 \text{ mm} \times 0.1 \text{ mm}$	$1 \mu\text{m} \times 1 \mu\text{m}$
Number of particles	$8 \times 10^5$	1
Shots per image	3000	1
Dose per image	$1.5 \times 10^{12}$	$10^{12}$
Scattering yield (arbitrary units)	1	0.54%

The experiments have been performed on an ensemble of particles of  $N \simeq 10^6$ . The data allowed vapor bubbles to be easily detected in the few nanometer range at rather short exposure times. The curves shown are single differentials based on a 3 s exposure time each. This still means that the quality of the structure information is limited to an ensemble average of different particle sizes and shapes. The Gaussian shape of the laser focus adds the dispersion in fluence, although the X-rays probe only the central part of the laser focus. Finally, 3000 individual pump–probe shots were accumulated for one data point, which adds the effects of pulse-to-pulse fluctuations of the laser intensity and the pointing stability. Generally one would like to perform an experiment without these limitations to obtain a higher resolution in time and space of the nanoscale dynamics. Schemes have been proposed to record the scattering patterns from single objects in the focused X-ray beam and reconstructing the real-space information by iterative phase retrieval (oversampling) (Miao *et al.*, 2005; Robinson *et al.*, 2001; He *et al.*, 2003; Marchesini *et al.*, 2003; Hau-Riege *et al.*, 2005; Jurek *et al.*, 2004; Eisebitt *et al.*, 2004). Recently this has been realised on larger colloidal objects using the soft X-ray emission of the Hamburg free-electron laser FLASH (Chapman *et al.*, 2006) in the fashion of a single-shot exposure.

Table 1 shows the relevant photon numbers of the present experiment and the future requirements for one-shot one-particle imaging. At present  $1.5 \times 10^{12}$  X-ray photons are used to produce the difference scattering intensity required for following the phase explosion dynamics of gold particles in water, which is comparable with the number of photons in one pulse at the XFEL. The illuminated volume contains  $8 \times 10^5$  particles. A reduction of the X-ray focal size to  $1 \mu\text{m}$  will allow the same signal to be obtained with less than 100 particles. Given the increase in X-ray flux at a future XFEL source one could obtain a similar scattering pattern (with a moderately lower signal-to-noise level) for a single gold particle in the beam, including the condensed phase medium. Thereby the full time resolution could be explored, avoiding shot-to-shot jitter between laser excitation and X-ray probe. This has been demonstrated for single-crystal diffraction on the linear accelerator at SLAC (Cavalieri *et al.*, 2005; Lindenberg *et al.*, 2005).

By using a droplet generator, one could excite particle suspensions without the need for containment, which will reduce the background. Focusing of the X-rays to  $1 \mu\text{m}$

diameter may be achieved by a combination of several devices. First, a toroidal mirror could provide an intermediate focus. State-of-the-art figured mirrors can provide a focus size of less than 50  $\mu\text{m}$  at moderate demagnification, which is still limited by the slope error of the surface profile rather than the source divergence at third-generation synchrotron insertion devices, such as at ID09 (Eybert *et al.*, 2002). The smaller footprint of the XFEL beam on the mirror (higher deflection angle, smaller divergence), together with a more sophisticated mirror design (active optics), could already pre-focus the beam to a 10  $\mu\text{m}$  size. An optional additional element could then provide a tighter focus (such as compound lenses or strongly curved mirrors).

The X-ray laser beam will display a much larger fraction of coherent radiation compared with synchrotron sources. While being transversely fully coherent, a larger number of longitudinal modes will be produced owing to the amplification of the spontaneous emission through the SASE principle. As a consequence the spectrum will be broadened to about 0.1% of the center energy. A consequence will be that, firstly, the resolution will not be extended to the atomic scale, while the mesoscale structure would still be completely obtained. Secondly, the large coherence length can create diffraction from larger length scales, such as fluctuations in the liquid phase or sample containment. They will, however, also be damped by the spectral broadening and separated on the  $Q$  scale from the particle's dimension.

A comparison of the signal-to-noise ratio (purely Poisson counting statistics, *i.e.* shot noise) with the expected intensity change due to a thin vapor layer forming on a single particle shows that the resolution limit can even be increased (Fig. 6). The shown measured data at a fluence of  $100 \text{ J m}^{-2}$  are limited to  $Q = 0.04 \text{ \AA}^{-1}$  owing to the smearing of the signal due to particle dispersion and laser fluence fluctuations, while at the same signal-to-noise ratio a two-times-higher resolution may be achieved by avoiding the ensemble averaging.

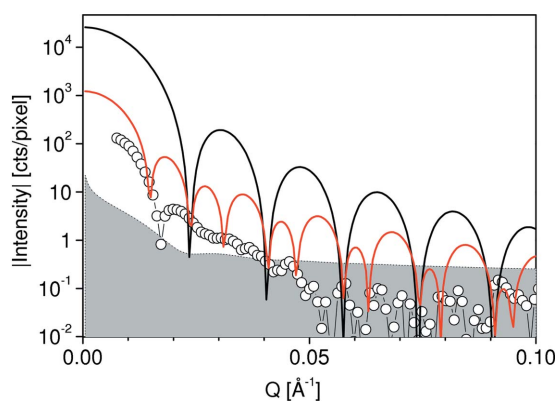


**Figure 6**

Calculation of the change of the scattering yield (modulus) owing to a thin sheet of vapor forming around a gold particle (red line, 2 nm vapor thickness on a 38 nm particle) compared with the signal-to-noise ratio limit owing to the shot noise (grey shaded area). The black line (uppermost curve) represents the full scattering of an ideal sphere, while the circles show the modulus of measured data of a 6 nm vapor layer on the ensemble of particles.

It should be noted that the increase in X-ray flux density by seven orders of magnitude will have a heavy impact on the integrity of the nanostructures. In the present experiment only 2% of all particles in the sample absorb an X-ray photon (one of which would increase the temperature of the particle by 200 K), which does not bias the results. In an XFEL experiment each particle would absorb almost  $10^6$  photons in 100 fs, which will lead to a violent Coulomb explosion (Wabnitz *et al.*, 2002; Neutze *et al.*, 2000; Hau-Riege *et al.*, 2005). Such a situation has been simulated for an organic molecule in a strongly focused X-ray beam by Neutze *et al.* (2000). The explosion within the duration of the X-ray radiation is predicted to be so rapid that it will compromise the quality of the scattering information. Estimations have been given for the relation between X-ray fluence and pulse duration to take advantage of the inertia of the system to complete the scattering before the explosion of the macromolecules. They concluded that, with  $10^{12}$  photons in a 100 nm spot, a pulse duration shorter than 50 fs would be needed for the imaging of a lysozyme molecule, while a much larger tolerance was calculated for a larger virus. Later, hydrodynamic code was used to understand better the dynamics of the emitted electrons and their secondary processes (Hau-Riege *et al.*, 2004, 2005). The conditions for biological objects are shown to be very severe with maximum tolerable pulse lengths of a few femtoseconds. This holds for biological matter with a large number of weakly bound electrons and for small clusters in the 10–20 nm region (Jurek *et al.*, 2004). For heavier atoms, such as gold or other metals, and also for embedded particles, the explosion reaction should be considerably slowed down (Shen *et al.*, 2004). Additionally, the mesoscale imaging would not require unperturbed electron configurations at the atomic positions as has been proposed for biological molecules.

## 6. Conclusion and outlook

We have presented pump–probe small-angle scattering experiments from photo-excited gold nanoparticles that provide structural information on the 100 ps time scale. With the standard set-up of the dedicated beamline ID09B at the ESRF, it was possible to follow the phase explosion dynamics of the liquid, as well as nanometric structural changes of the particles. The scattering set-up is efficient enough to project experiments with single-pulse excitation or even single-particle imaging with future light sources.

This work is supported by the German Science Foundation DFG through the SFB 513 and the Center for Junior Research Fellows of the University of Konstanz. We would like to acknowledge valuable input and help from Q. Kong, M. Cammarata, G. von Plessen and M. Lorenc.

## References

- Aghababian, A. *et al.* (2006). *XFEL – The European X-ray Free-Electron Laser, Technical Design Report*, edited by M. Altarelli *et al.* DESY 06-097, Hamburg, Germany.

- Arthur, J. *et al.* (2002). SLAC Internal Report SLAC-R-593. Linac Coherent Light Source Conceptual Design Report, SLAC, Menlo Park, CA, USA.
- Cao, J., Ihee, H. & Zewail, A. H. (1999). *Proc. Natl. Acad. Sci.* **96**, 338–342.
- Cavalleri, A. L. *et al.* (2005). *Phys. Rev. Lett.* **94**, 114801.
- Chapman, H. N. *et al.* (2006). *Nature Phys.* **2**, 839–843.
- Chen, L., Jäger, W. J. H., Jennings, G., Gosztola, D. J., Munkholm, A. & Hessler, J. P. (2001). *Science*, **292**, 262–264.
- Collet, E., Lemée-Cailleau, M.-H., Buron-Le Cointe, M., Cailleau, H., Wulff, M., Luty, T., Koshihara, S.-Y., Meyer, M., Toupet, L., Rabiller, P. & Techert, S. (2003). *Science*, **300**, 612–615.
- Debye, P. (1929). *Polar Molecules*. London: Dover.
- Dingenouts, N., Bolze, J., Pötschke, D. & Ballauff, M. (1999). *Adv. Polym. Sci.* **144**, 1–47.
- Eisebitt, S. *et al.* (2004). *Nature (London)*, **432**, 883–888.
- Eybert, L., Wulff, M., Reichenbach, W., Plech, A., Schotte, F., Gagliardini, E., Zhang, L., Hignette, O., Rommeveaux, A. & Freund, A. (2002). *Proc. SPIE*, **4782**, 246.
- Guinier, A. & Fournet, G. (1955). *Small-Angle Scattering of X-rays*. New York: John Wiley & Sons.
- Hammersley, A. P., Svensson, S. O., Hanfland, M., Fitch, A. & Häusermann, D. (1996). *High Press. Res.* **14**, 235–248.
- Hau-Riege, S. P., London, R. A., Hultdt, G. & Chapman, H. N. (2005). *Phys. Rev. E*, **71**, 061919.
- Hau-Riege, S. P., London, R. A. & Szöke, A. N. (2004). *Phys. Rev. E*, **69**, 051906.
- He, H., Marchesini, S., Howells, M., Weierstall, U., Chapman, H., Hau-Riege, S., Noy, A. & Spence, J. C. H. (2003). *Phys. Rev. B*, **67**, 174114.
- Hu, M., Petrova, H. & Hartland, G. V. (2004). *Chem. Phys. Lett.* **391**, 220–225.
- Ihee, H., Lorenc, M., Kim, T. K., Kong, Q. Y., Cammarata, M., Lee, J. H., Bratos, S. & Wulff, M. (2005). *Science*, **309**, 1223–1227.
- Jurek, Z., Oszlányi, G. & Faigel, G. (2004). *Europhys. Lett.* **65**, 491–497.
- Kimling, J., Maier, M., Okenve, B., Kotaidis, V., Ballot, H. & Plech, A. (2006). *J. Phys. Chem. B*, **110**, 15700–15707.
- Kotaidis, V., Dahmen, C., von Plessen, G., Springer, F. & Plech, A. (2006). *J. Chem. Phys.* **124**, 184702.
- Kotaidis, V. & Plech, A. (2005). *Appl. Phys. Lett.* **87**, 213102.
- Lindenberg, A. M. *et al.* (2005). *Science*, **308**, 392–395.
- Link, S. & El-Sayed, M. A. (2000). *Int. Rev. Phys. Chem.* **19**, 409–453.
- Maillard, M., Pileni, M. P., Link, S. & El-Sayed, M.-A. (2004). *J. Phys. Chem. B*, **108**, 5230–5234.
- Marchesini, S., He, H., Chapman, H. N., Hau-Riege, S. P., Noy, A., Howells, M. R., Weierstall, U. & Spence, J. C. H. (2003). *Phys. Rev. B*, **68**, 140101.
- Miao, J., Nishino, Y., Kohmura, Y., Johnson, B., Song, C., Risbud, S. H. & Ishikawa, T. (2005). *Phys. Rev. Lett.* **95**, 085503.
- Neutze, R., Wouts, R., van der Spoel, D., Weckert, E. & Hajdu, J. (2000). *Nature (London)*, **406**, 752–757.
- Pitsillides, C. M., Joe, E. K., Wei, X., Anderson, R. R. & Lin, C. P. (2003). *Biophys. J.* **84**, 4023–4032.
- Plech, A., Kotaidis, V., Lorenc, M. & Boneberg, J. (2006). *Nature Phys.* **2**, 44–47.
- Plech, A., Kotaidis, V., Lorenc, M. & Wulff, M. (2005). *Chem. Phys. Lett.* **401**, 565–569.
- Plech, A., Randler, R., Geis, A. & Wulff, M. (2002). *J. Synchrotron Rad.* **9**, 287–292.
- Plech, A., Wulff, M., Bratos, S., Mirloup, F., Vuilleumier, R., Schotte, F. & Anfinrud, P. A. (2004). *Phys. Rev. Lett.* **92**, 125505.
- Pollack, L., Tate, M. W., Finnefrock, A. C., Kalidas, C., Trotter, S., Darnton, N. C., Lurio, L., Austin, R. H., Batt, C. A., Gruner, S. M. & Mochrie, S. G. J. (2001). *Phys. Rev. Lett.* **86**, 4962–4965.
- Robinson, I. K., Vartanyants, I. A., Williams, G. J., Pfeifer, M. A. & Pitney, J. A. (2001). *Phys. Rev. Lett.* **87**, 195505.
- Rousse, A., Rischel, C. & Gaultier, J.-C. (2001). *Nature (London)*, **410**, 65–68.
- Saes, M., Bressler, C., Abela, R., Grolimund, D., Johnson, S. L., Heimann, P. A. & Chergui, M. (2003). *Phys. Rev. Lett.* **90**, 047403.
- Schotte, F., Lim, M., Jackson, T. A., Smirnov, A. V., Soman, J., Olson, J. S., Phillips, G. N. Jr, Wulff, M. & Anfinrud, P. A. (2003). *Science*, **300**, 1944–1947.
- Schotte, F., Techert, S., Anfinrud, P. A., Srajer, V., Moffat, K. & Wulff, M. (2002). In *Third-Generation Hard X-ray Synchrotron Radiation Sources*, edited by D. Mills. New York: John Wiley & Sons.
- Shen, Q., Bazarov, I. & Thibault, P. (2004). *J. Synchrotron Rad.* **11**, 432–438.
- Siders, C. W., Cavalleri, A., Sokolowski-Tinten, K., Toeth, Cs., Guo, T., Kammler, M., Horn von Hoegen, M., Wilson, K. R., von der Linde, D. & Barty, C. P. J. (1999). *Science*, **286**, 1340–1342.
- Techert, S., Schotte, F. & Wulff, M. (2001). *Phys. Rev. Lett.* **86**, 2030–2033.
- Turkevich, J., Stevenson, P. C. & Hillier, J. (1951). *Discuss. Faraday Soc.* **11**, 55.
- Wabnitz, H. *et al.* (2002). *Nature (London)*, **420**, 482–485.
- Wagner, J. (2004). *J. Appl. Cryst.* **37**, 750–756.